Nuclear Inst. and Methods in Physics Research, A 984 (2020) 164599

Contents lists available at ScienceDirect

Nuclear Inst. and Methods in Physics Research, A

journal homepage: www.elsevier.com/locate/nima

A magneto-mechanical model for rotating-coil magnetometers

Stefano Sorti [a,b,*], Carlo Petrone [a], Stephan Russenschuck [a], Francesco Braghin [b]

[a] CERN, European Organization for Nuclear Research, CH-1211 Geneva 23, Switzerland
[b] Politecnico di Milano, Dipartimento di Meccanica, via La Masa 1, 20156 Milano, Italy

ARTICLE INFO

Keywords:
Magnetic measurements
Magnetic field
Timoshenko theory
Rotating-coil magnetometers
Rotating shaft

ABSTRACT

Rotating-coil magnetometers are among the most common transducers for measuring local and integral magnetic fields of accelerator magnets. The measurement uncertainty strongly depends on the mechanical properties of the shafts, bearings, drive systems, and supports. This paper proposes an analytical mechanical model for rotating-coil magnetometers, which allows a sensitivity analysis of mechanical phenomena affecting magnetic measurements. Both static and dynamic effects are considered. The model is validated numerically with a finite element model, and experimentally on an operational device.

1. Introduction

Magnet production follow-up requires several field measurements at various states of completion, after collaring, yoking, and cryostat integration. Magnetic measurements are providing feedback to the magnet designer, guarantee the magnet-to-magnet reproducibility, and are used for optimizing the accelerator performance. In most cases, however, the measurement of the integrated field quality is sufficient [1] and local field maps are not required.

Rotating-coil magnetometers are the most common transducers for measuring the field quality inside the bore of magnets for charged-particle accelerators. Rotating-coil measurements belong to the family of *induction-coil* transducers that are based on Faraday's law of induction, featuring one or more induction coils mounted on a mechanical support shaft that is aligned with the longitudinal axis of the magnet. The induced voltage in each coil is proportional to the rate-of-change of the flux linked with the coil surface. In general the shafts (or shaft chains) are long enough to cover the entire length of the magnet, including its fringe-field regions.

Rigidly fixed onto the shaft, the induction coils undergo the typical mechanical phenomena affecting a rotating beam, like static and dynamic forces, and misalignment. The control of the mechanical properties in the shaft design [2] and mechanical vibrations during the operation [3] are crucial for the measurement results. Typically, a shaft and its support are designed to have natural frequencies higher than the operating frequencies [4]. Basic mechanical formulae are suited only for phenomena such as deformation under gravity. Transverse and torsional vibrations were already taken into account for rotating-coil models in Ref. [5], although a mechanical description of the shaft body is missing. However, mechanical phenomena have a dominating impact on the measurement uncertainty compared to the electronic components in the data-acquisition system [6]. A mitigation of the mechanical effects is a signal-compensation technique known as *bucking* [7], which strongly depends on the construction techniques of the coils. Coils made in Printed Circuit Board (PCB) technology are far more reproducible then hand-wound coils that are more appropriate for a large number of turns. A model to quantify the mitigation effect of the bucking is still missing and therefore the main goal of this work.

This paper provides a complete coupling model between mechanical effects and magnetic measurement results. The model is appropriate for both the design and the operation of rotating-coil magnetometers. In particular, Section 2 addresses the mechanical model of the rotating-coil shaft, consisting of an analytical model of a Timoshenko beam on elastic supports. It also covers the geometrical description of the coil and its coupling with the shaft. Section 3 introduces the description of the magnetic flux density and figure of merit of the system design. Section 4 covers the numerical and experimental validations of the model. Finally, Section 5 is devoted to a general sensitivity analysis of an operational coil magnetometer, based on the developed model.

2. The mechanics of the coil shaft

The mechanical model of rotating-coil magnetometers is based on the following hypotheses:

- A magnetometer is a flexible shaft supported by two ideal bearings, modelled as lumped elements.
- The shaft material is homogeneous and linear elastic.

* Corresponding author at: CERN, European Organization for Nuclear Research, CH-1211 Geneva 23, Switzerland.
E-mail address: stefano.sorti@cern.ch (S. Sorti).

https://doi.org/10.1016/j.nima.2020.164599
Received 11 June 2020; Received in revised form 6 August 2020; Accepted 1 September 2020
Available online 12 September 2020

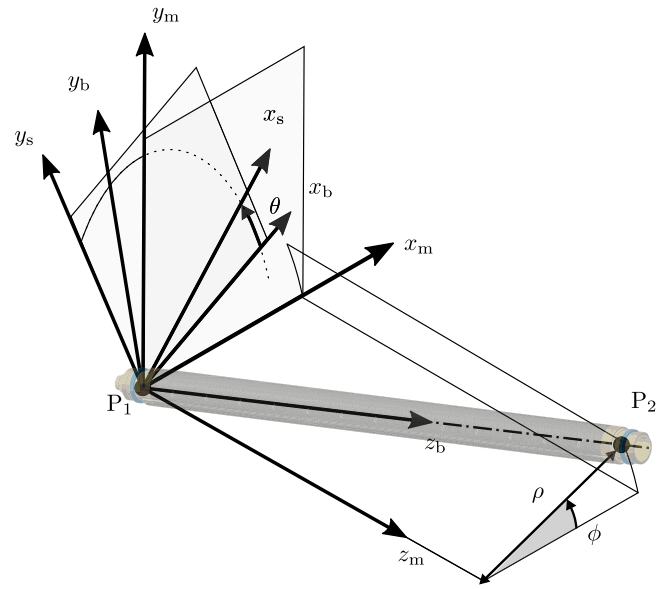

Fig. 1. Main coordinate systems to express rotating-coil axis misalignment, identified by the segment connecting the bearing points P_1 and P_2. The coordinate systems introduced are: the magnet frame (m), here shown with its origin already shifted into P_1, its rotation to align it with the bearings (b) and the local frame rotating with the shaft (s). ρ and ϕ express the misalignment of the bearing and magnet axes.

- Axial, torsional, and flexural vibrations are decoupled. Only flexural vibrations are considered, being the most critical ones. Axial and torsional modes are computed using FEM to verify this assumption.
- The rotation speed is slow enough ($\lesssim$8 Hz) to neglect rotordynamics phenomena, such as the gyroscopic effect. The rotation speed is expected to be well below the first critical speed. Nevertheless, shaft eccentricity is introduced as an external force acting on the shaft.
- The rotation speed is not constant, so that the angular displacement, known a priori, becomes a function of time. This assumption allows to include non-uniform velocities, particularly transients to start and stop rotation, to describe the shaft motion during flip-coil measurements [8].

The Timoshenko theory, applied in this paper, is an appropriate model for torsional dynamics, layered composite shafts, and multi-segment rotating beams [9–12]. The main advantage with respect to the common Euler–Bernoulli theory is the possibility to model beams with a short length, compared to the cross-section width [13].

The misalignment of the rotation axis and shaft deformation are the two main aspects for the mechanical characterization of rotating coils. The rigid misalignment is expressed using a coordinate transformation, and the shaft deformation through the application of the Timoshenko theory.

2.1. Shaft misalignment

Coordinate-system transformations are used to express the misalignment between the magnet and shaft axes. As shown in Fig. 1, the coordinate systems are:

- (x_m, y_m, z_m) is the ***magnet coordinate frame***, in which the field distribution and all measurement results are expressed. Its origin is located at the centre of the magnet axis (which is a parameter of the magnet). To avoid overloading Fig. 1 this frame is shown already translated into one of the shaft bearings; P_1.

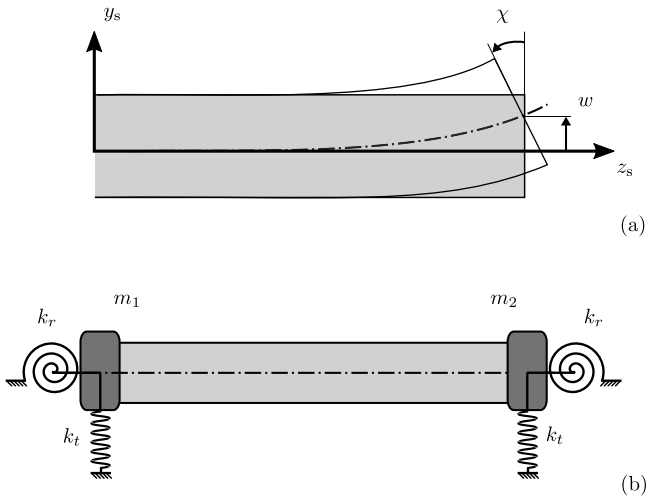

Fig. 2. Timoshenko beam for each of the two principal directions (pictured along y_s). It represents the variables to solve for, in order to obtain the deformation field (a) and the boundary conditions to apply at bearings (b). Elements k and m are lumped spring and mass elements.

- (x_b, y_b, z_b) is the ***bearing coordinate frame***. It is identified by the translation of (x_m, y_m, z_m) into P_1, followed by a rotation to align z_b with the shaft axis, that is, the segment from P_1 to P_2.
- (x_s, y_s, z_s) is the ***shaft coordinate frame***. It is obtained by the rotation of (x_b, y_b, z_b) around z_b and thus solidly moves with the shaft.

The bearing P_1, is supposed to be on the axis of the magnet. The transformation from the magnet coordinate frame to the bearing coordinate frame consists of a translation and two rotations about axes. The first is performed around y_m by an angle of α_1, identifying the temporary coordinates (x_t, y_t, z_t). The second rotation is performed around the x_t axis by an angle of α_2, so that z_t coincides with the direction of the segment P_1P_2. Instead of using α_1 and α_2, it is proposed to express the misalignment by a radial misalignment ρ and its spatial phase ϕ.

Finally, the shaft coordinate frame is identified through the angular displacement $\theta(t)$, as shown in Fig. 1. Therefore it is possible to write the overall relationship accounting for shaft misalignment and rotation. Given a generic point of coordinates $\boldsymbol{x}_s$, it results in

$$\boldsymbol{x}_s = T\ R_\theta(t)\ R(\rho, \phi)\ \boldsymbol{x}_m, \tag{1}$$

where $R_\theta(t)$ and $R(\rho, \phi)$ are rotation matrices for shaft motion and misalignment and T is the translation matrix.

2.2. Shaft deformations

Shaft deformations are modelled in the shaft coordinate frame. In this way, the principal directions of the shaft are identified as fixed in space and can be modelled separately. The quantity of interest is the three-dimensional deformation field of the shaft body $\boldsymbol{u}$. This is a function of the displacement w and rotation angle χ of the beam cross-section, as shown in Fig. 2a. Based on Timoshenko's equations [13], it is possible to write for small deformations:

$$\boldsymbol{u}(x, y, z, t) = \begin{bmatrix} w_x(z,t) \\ w_y(z,t) \\ x\chi_y(z,t) - y\chi_x(z,t) \end{bmatrix}, \tag{2}$$

where the subscripts denote the variables, solved independently in the xz- and yz-planes. To save on notation, the subscripts are omitted in what follows.

Each principal direction is analysed separately, reducing the three-dimensional problem to a pair of planar beams. This assumption is

valid as long as rotor-dynamics can be neglected. Otherwise, coupling between planes may arise from asymmetry, in which case the general approach remains valid, but extra terms appear [14]. The proposed analysis starts with the free motion of the system to identify the modes of vibration.

2.3. Shaft deformations: free motion

A beam in the $y_s z_s$-plane is now considered. The first step in the vibration analysis is the free, undamped response of the system. It allows for the characterization of the dynamic behaviour of the shaft, as the baseline for a more complete study of damped, forced motion. With $\boldsymbol{v}(z,t) = (w(z,t),\ \chi(z,t))$, the free motion of a Timoshenko beam satisfies the one dimensional wave equation [9]

$$M\frac{\partial^2 \boldsymbol{v}}{\partial t^2}(z,t) + K\boldsymbol{v}(z,t) = 0, \tag{3}$$

where

$$M = \begin{bmatrix} \rho A & 0 \\ 0 & \rho I \end{bmatrix}, \quad K = AG\kappa \begin{bmatrix} -\frac{\partial^2}{\partial z^2} & \frac{\partial}{\partial z} \\ -\frac{\partial}{\partial z} & 1 - \frac{EI}{AG\kappa}\frac{\partial^2}{\partial z^2} \end{bmatrix}, \tag{4}$$

E is the Young's modulus, I and A are the momentum of inertia and the area of the shaft cross-section, G is the shear modulus, ρ the material density, and κ the shear constant. For a simple geometry, well-assessed formulas for κ exist [15]. For more complicated ones, numerical methods are necessary [16].

A solution of Eq. (3) can be approached by a Fourier transformation. Consider

$$w(z,t) = W(z)\eta(t), \qquad \chi(z,t) = X(z)\eta(t), \tag{5}$$

where $W(z)$ and $X(z)$ are modal shapes with physical unit $[W(z)] = 1$ m and $[X(z)] = 1$ rad, and $\eta(t)$ are the modal coordinates, with $[\eta(t)] = 1_{\mathrm{U}}$. The solution for $\eta(t)$ is imposed to be harmonic, with an angular frequency ω. Eqs. (5) are substituted into Eq. (3) to obtain

$$W^{(2)}(z) + \underbrace{\frac{\omega^2\rho}{\kappa G}}_{a} W(z) - X'(z) = 0\,, \tag{6a}$$

$$X^{(2)}(z) + \underbrace{\left(\frac{\omega^2\rho}{E} - \frac{AG\kappa}{EI}\right)}_{b} X(z) + \underbrace{\frac{AG\kappa}{EI}}_{c} W'(z) = 0\,, \tag{6b}$$

$$\ddot{\eta}(t) + \omega^2\eta(t) = 0\,. \tag{6c}$$

Rearranging and differentiating the first and the second equations, it is possible to write

$$W^{(4)}(z) + \underbrace{(a+b+c)}_{d} W^{(2)}(z) + \underbrace{ab}_{e} W(z) = 0\,. \tag{7}$$

Solutions for Eq. (7) can be written in the form $W(z) = \sum_{i=1}^{4} P_i e^{\lambda_i z}$. The coefficients λ_i stem from the solution of the characteristic polynomial and are functions of the angular frequency ω. The coefficients P_i of the fourth-order equation are determined by the boundary conditions. For each ω, which is a natural frequency of the system, a modal-shape function $W(z)$ can be found.

Fig. 2b shows the boundary conditions for a *generally-supported beam* model [13]. This support prescribes a transversal (k_t) and a torsional (k_r) spring at the two ends, including two lumped masses (m_1, m_2) and inertias (J_1, J_2). The boundary conditions impose the equilibrium between the internal forces (shear T and momentum M), the spring forces, and the inertias at each end. In particular, at $z = 0$,

$$M = EI\frac{\partial \chi}{\partial z} = -k_r\frac{\partial w}{\partial z} - J_1\frac{\partial^2 \chi}{\partial t^2}\,, \tag{8a}$$

$$T = AG\kappa\left(\frac{\partial w}{\partial z} - \chi\right) = k_t w + m_1\frac{\partial^2 w}{\partial t^2}\,. \tag{8b}$$

At $z = L$, where L is the shaft length, the signs of the lumped elements are reversed and the mass m_1 substituted by m_2. Fourier transformation (Eq. (5)) is applied to Eqs. (8). Together with the boundary conditions at $z = L$, the ones at $z = 0$ form a system of equations that can be written as

$$\begin{bmatrix} & A(\omega) & \end{bmatrix} \begin{bmatrix} P_1 \\ P_2 \\ P_3 \\ P_4 \end{bmatrix} = 0\,. \tag{9}$$

Non-trivial solutions for this linear equation system require that $\det(A(\omega)) = 0$. Let ω_n identify the solutions for the nth natural frequency. For each ω_n, the coefficients $P_{i,n}$ can be computed to obtain the expression of $W_n(z)$. To compute the modal shapes $X_n(z)$, Eq. (6a) is differentiated in z and inserted into Eq. (6b). Because $W_n(z)$ and $X_n(z)$ are the eigenvectors of the problem, their scaling is arbitrary. Therefore, the so-called mass normalization is performed [9]. The definition of the modal masses $m_{\eta,n}$ for the nth mode is given as

$$m_{\eta,n} = \int_0^L \boldsymbol{U}_n^{\mathrm{T}} M \boldsymbol{U}_n \mathrm{d}z, \tag{10}$$

where $\boldsymbol{U}_n$ is the vector of modal shapes ($W_n(z)$ and $X_n(z)$). The modal shapes are thus scaled to yield unitary modal masses. This is coherent with the formulation of Eq. (6c), where the mass is unitary and the stiffness is equal to ω^2.

2.4. Shaft deformations: forced motion

Considering damping and external forces, the one-dimensional wave equation becomes

$$M\frac{\partial^2 \boldsymbol{v}}{\partial t^2}(z,t) + C\frac{\partial \boldsymbol{v}}{\partial t}(z,t) + K\boldsymbol{v}(z,t) = \boldsymbol{f}(z,t)\,. \tag{11}$$

Damping is introduced as Rayleigh damping [17] containing mass and stiffness proportional, empirical parameters α and β:

$$C = \alpha M + \beta K. \tag{12}$$

The forces and momenta are distributed and written as $f(z,t)$ and $\mu(z,t)$, with physical units of $[f(z,t)] = 1$ N/m^{-1} and $[\mu(z,t)] = 1$ N. For each mode n, the so-called modal forces and momenta are

$$f_n(t) = \int_0^L W_n(z) f(z,t)\mathrm{d}z, \tag{13a}$$

$$\mu_n(t) = \int_0^L X_n(z)\mu(z,t)\mathrm{d}z\,. \tag{13b}$$

In this way, the most common excitation functions can be introduced directly as modal forces. For instance, a generic harmonic excitation of amplitude F_0, characterized by frequency ω_{f} and phase ψ_{f}, at a certain point z_{f},[1] is written as

$$\begin{aligned} f_n(t) &= \int_0^L F_0 W_n(z)\delta(z - z_{\mathrm{f}})\cos\left(\omega_{\mathrm{f}}t + \psi_{\mathrm{f}}\right)\mathrm{d}z = \\ &= \underbrace{F_0 W_n(z_{\mathrm{f}})}_{F_n}\cos\left(\omega_{\mathrm{f}}t + \psi_{\mathrm{f}}\right)\,. \end{aligned} \tag{14}$$

Because the modes are orthogonal, each modal coordinate function can be solved separately by

$$\ddot{\eta}_n(t) + c_n\dot{\eta}_n(t) + \omega_n^2\eta_n(t) = F_n\cos\left(\omega_{\mathrm{f}}t + \psi_{\mathrm{f}}\right)\,, \tag{15}$$

where c_n is the modal damping. The solution is of the form

$$\eta_n(t) = A_n\cos\left(\omega_{\mathrm{f}}t + \psi_n\right)\,, \tag{16}$$

[1] Subscript f denotes the force parameters.

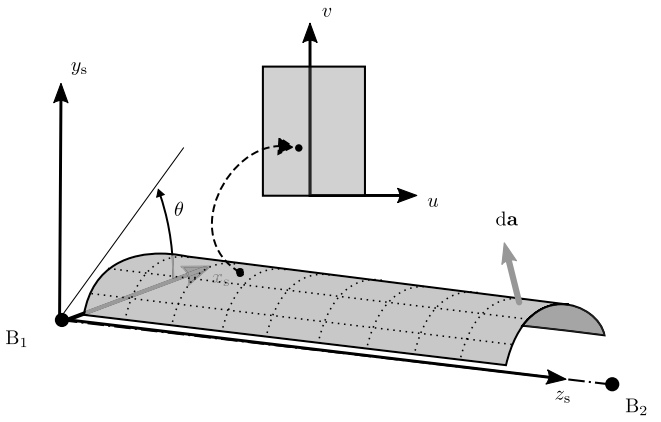

Fig. 3. Definition of the coil geometry and its parametric representation. Coil geometry is a surface, taken as a sub-set of the shaft volume. In the figure, the full body of the shaft is omitted for clarity. Moreover, despite coils are mostly flat surfaces, the one in the figure is curved, to highlight that the model can accept any coil geometry.

where A_n and ψ_n are modal amplitude and phase. The deformation field of Eq. (2) can then be written in modal form as:

$$\boldsymbol{u} = \sum_{n=1}^{N} \begin{bmatrix} 0 & W_{x,n} \\ W_{y,n} & 0 \\ xX_{y,n} & -yX_{x,n} \end{bmatrix} \begin{bmatrix} A_{y,n}\cos(\omega_f t + \psi_{y,n}) \\ A_{x,n}\sin(\omega_f t + \psi_{x,n}) \end{bmatrix}, \tag{17}$$

where the highest considered mode is ω_N chosen such that $\omega_N \gg \omega_f$.

It is important to recall that the dynamics of the shaft is expressed in the shaft coordinate frame. Therefore, also the excitations must be expressed in this frame.

2.5. The coil geometry

The coil geometry is modelled as a surface in the shaft coordinate frame. The vector $\boldsymbol{c}_u$ describes the undeformed position of the mass points, expressed as a function of the two local parameters (u, v), and therefore written as $\boldsymbol{c}_u(u, v)$.

The deformation field of the shaft is linearly superimposed to the plain coil geometry as

$$\boldsymbol{c}(u, v) = \boldsymbol{c}_u(u, v) + \boldsymbol{u}(\boldsymbol{c}_u(u, v)), \tag{18}$$

where $\boldsymbol{c}$ is the deformed coil geometry. Its surface element is

$$\mathrm{d}\boldsymbol{a} = -\frac{\partial \boldsymbol{c}(u, v)}{\partial u} \times \frac{\partial \boldsymbol{c}(u, v)}{\partial v} \mathrm{d}u\mathrm{d}v, \tag{19}$$

see Fig. 3. Consider now a rectangular coil, parallel to the $x_s z_s$-plane, with an elevation h. The coil geometry is described by the position vector $\boldsymbol{c} = (u, h, z)$, mapped to a rectangle in the local coordinates (u, v). If, for example, the deformation field of the shaft is the one of Eq. (17), the coil geometry can be described as

$$\boldsymbol{c} = \begin{bmatrix} u \\ h \\ v \end{bmatrix} + \sum_{n=1}^{N} \begin{bmatrix} 0 & W_{x,n} \\ W_{y,n} & 0 \\ hX_{y,n} & -uX_{x,n} \end{bmatrix} \begin{bmatrix} A_{y,n}\cos(\omega_f t + \psi_{y,n}) \\ A_{x,n}\sin(\omega_f t + \psi_{x,n}) \end{bmatrix}. \tag{20}$$

3. Uncertainty of the measured magnetic-field components

The flux density in the aperture of a magnet, free of current sources and magnetic material can be expressed by a 3D Fourier–Bessel series [18]. Assuming an ideal quadrupole field over 60% of the shaft length, and a field roll-off that can be well described by the Enge function over a length of 5 times the magnet aperture radius, the field harmonics integrated over the entire length of the induction coil obeys the two-dimensional Laplace equation. The harmonic content can thus be written in the complex notation as $C_n^a(r_0) = B_n^a(r_0) + iA_n^a(r_0)$ expressed at the reference radius r_0.

3.1. The measurement procedure

The flux linkage in the coils is calculated with

$$\boldsymbol{\Phi} = \int_{\mathscr{A}} \boldsymbol{B} \cdot \mathrm{d}\boldsymbol{a}, \tag{21}$$

with $\mathrm{d}\boldsymbol{a}$ from Eq. (19). The flux is computed for the geometry of the deformed coil as determined by the mechanical dynamics. In a discrete setting, the flux increments $\boldsymbol{\Phi}_m$ for the M angular positions θ_m can be developed into a discrete Fourier series

$$\boldsymbol{\Psi}_n = \sum_{m=0}^{M-1} \boldsymbol{\Phi}_m \, e^{\frac{-i2\pi mn}{M}}. \tag{22}$$

This yields the harmonic content of the system response

$$C_n^a(r_0) = {r_0}^{n-1} \frac{\boldsymbol{\Psi}_n}{k_n}. \tag{23}$$

The terms k_n are the coil sensitivity factors for the nth field harmonic:

$$k_n = \frac{NL}{n}\left(r_2^n - r_1^n\right), \tag{24}$$

where N is the number of coil turns, L the total length of the coil and the two radii are the position of the go and return wire of the coil. The k_n express the integral sensitivity of the coil with respect to the multipole order n and as therefore not a function of z. The difference between the integrals over the imposed field harmonics and the apparent A_n^a, B_n^a coefficients is the main figure of merit to evaluate the geometrical deformations in the coil.

The sensitivity factors k_n are computed from the nominal values of the coil. In order to improve the accuracy of the measurement, the sensitivity factors are usually calibrated in a homogeneous dipole field and may thus include mechanical deformation. Using calibrated sensitivity factors would, however, not be beneficial for our study.

4. Model validation

Because the mechanical model includes some hypotheses and empirical parameters, an experimental validation of the mechanical model is performed in two steps: first, the beam model is compared with a production rotating-coil magnetometer, whose mechanics is experimentally characterized. The beam model is then compared with a finite-element model (FEM) of an existing shaft. The aim is to assess if the resulting mechanical effects are consistent. So why not limiting ourselves to the more complete FEM solution? The FEM model is "expensive" both in setup time as well as computation time compared to the proposed beam model, which is thus also suitable for a sensitivity analysis and optimization of the shaft design. Although a final refinement of a rotating-coil design should always undergo a proper FEM analysis, the aim of this paper is to identify the important design and material parameters and to derive an analytical transfer function between the shaft mechanics and the results of the magnetic measurement.

The reference is the rotating-coil magnetometer shown in Fig. 4. Table 1 lists its main properties. Material parameters are given by the manufacturer, while the geometrical and inertial parameters are calculated based on technical drawings. An equivalent mass density ρ is calculated to include all the additional elements (like bars and joints) in the shaft. The validity of this equivalent parameter is due to the homogeneous distribution of these elements along the shaft. A shear correction factor is obtained with a 2D numerical evaluation of the cross-section using commercial software [16]. The results are $k_x = 0.69$ and $k_y = 0.24$. The shaft length is $L = 1.52\,\mathrm{m}$, the bearing supports add masses of $m_1 = 0.58\,\mathrm{kg}$, and inertias of $J_1 = 7.92 \cdot 10^{-4}\,\mathrm{kg\,m^2}$ in $z_s = 0$, and $m_2 = 0.68\,\mathrm{kg}$ and $J_2 = 7.42 \cdot 10^{-4}\,\mathrm{kg\,m^2}$ in $z_s = L$. These parameters are based on the design drawings.

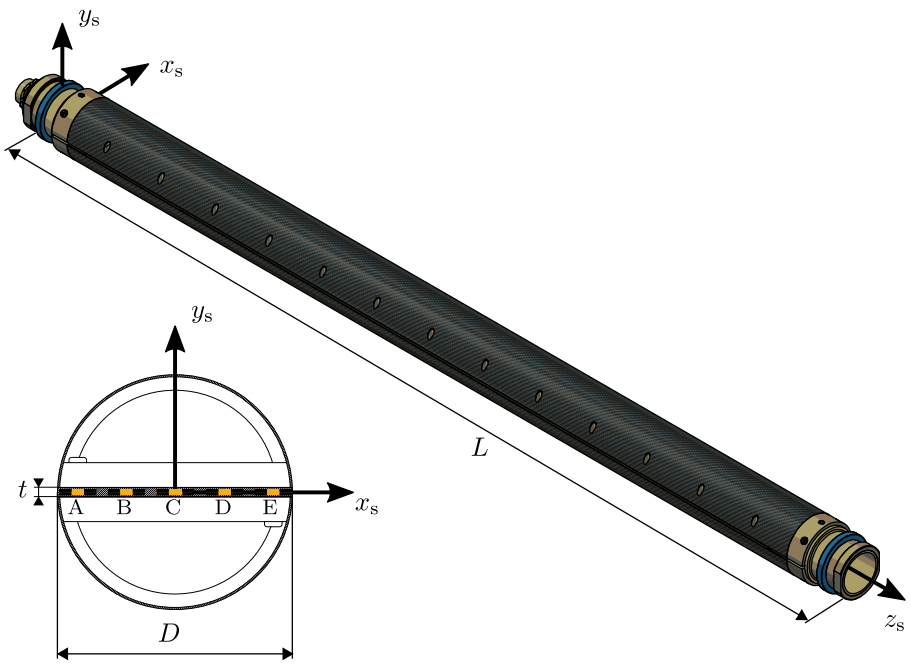

Fig. 4. The existing rotating-coil shaft of $L = 1.52\,\text{m}$ is used for the validation of the mechanical model. The shaft is made of two external half shells of diameter $D = 96\,\text{mm}$, in carbon fibre, fixing a Printed Circuit Board (PCB) of thickness $t = 3.7\,\text{mm}$. The PCB board contains five induction coils for measuring quadrupoles (orange rectangles in the cross-section view, identified by the letters A to E). Thirteen rigid bars are mounted inside the shaft in the direction of x_s to prevent deformations in the cross-section plane. Their effect was computed in FEM to confirm the assumption of a rigid cross-section in the beam model.

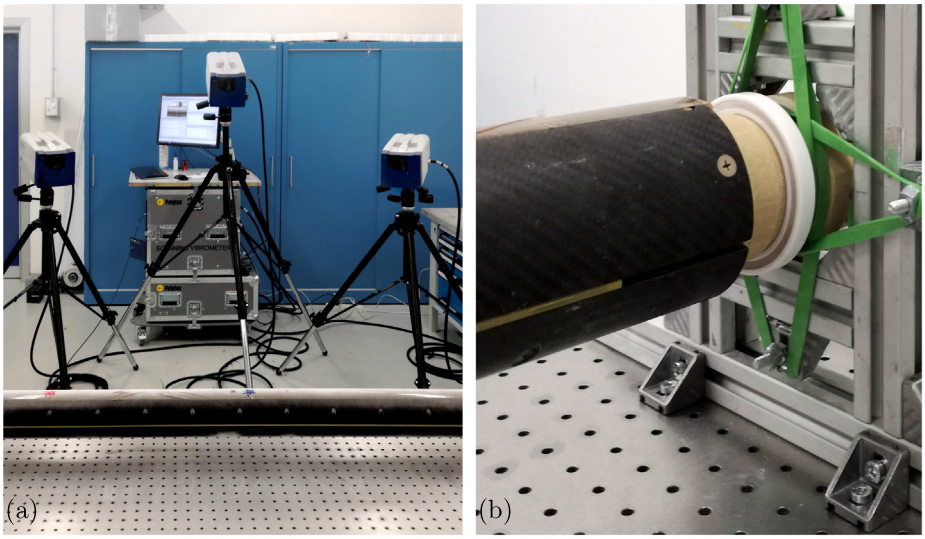

Fig. 5. The vibrometer set-up, with its acquisition system (a) and detail of the elastic support of the shaft (b). The white ring next to the rubber bands is the bearing.

Table 1
Properties of the rotating-coil shaft LHCMMWEQ0489.

Param.	E	G	ρ	A	I_x	I_y	I_t
Units	GPa	GPa	kg/m^3	cm^2	cm^4	cm^4	cm^4
CFRP	100	5	1550	3.55	33.7	33.7	67.3
FR4	20	9	1850	2.91	0.041	27.3	0.152
Av.	56	5.1	2892	6.46	60.1	69.8	120

(CFRP is Carbon fibre reinforced polymer, FR4 is the PCB resin, Av. denotes equivalent shaft properties).

Table 2
Coil parameters of LHCMMWEQ0489.

Coil n.	Turns n.	Coil start	Coil end	Spacing	Coil width
N_c	N_t	Z_1	Z_2	w_c	W
5	10	0.1 m	1.416 m	0.02 m	0.0102 m

4.1. Experimental validation of the shaft mechanics

The validation of the mechanical model is performed in two steps, involving both time-domain and frequency domain-signals for modal analysis [19,20]. In the first step, the shaft is suspended on rubber bands that provide almost ideal elastic boundary conditions. The second part of the test is performed with the shaft mounted on its actual bearings, which aims at investigating the validity of the support boundary conditions in the model.

As the shaft is not rotated during the tests, each plane is validated independently by external excitation with an impact hammer (PCB

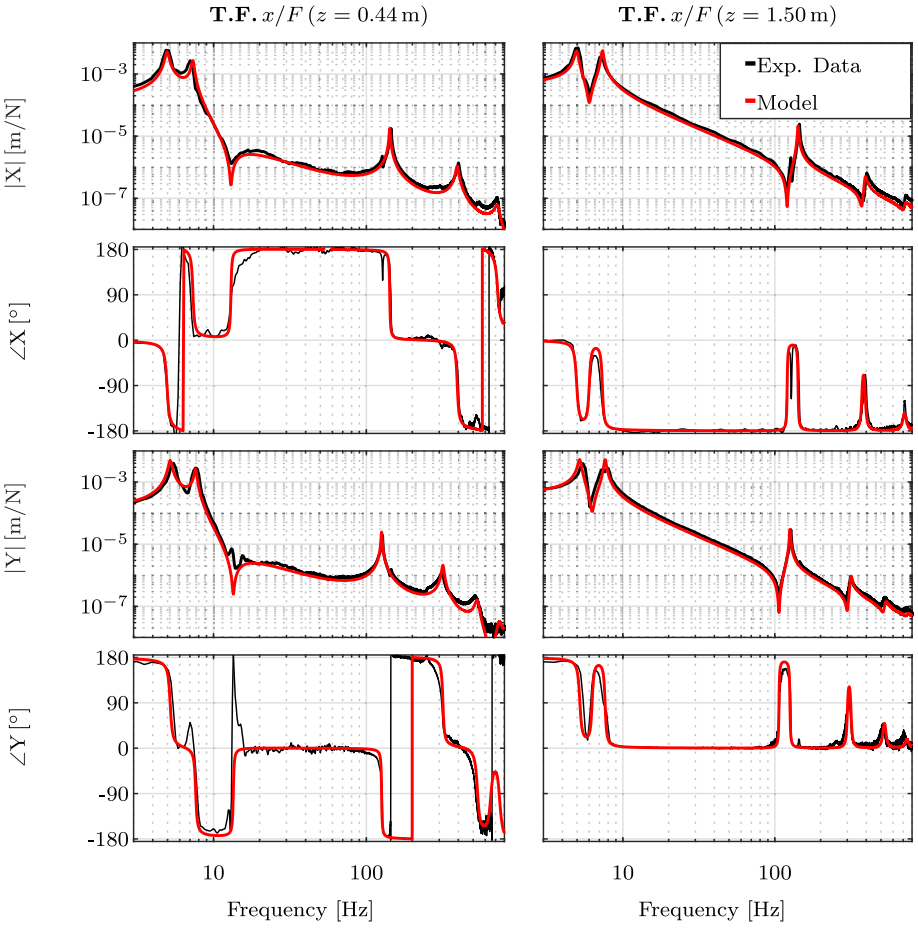

Fig. 6. Transfer functions of two sample points due to hammer excitation, in $+x$ and $-y$ direction. The frequency range involves the two rigid body motions and the first three bending modes. The driving point is $z = 1.50$ m (right).

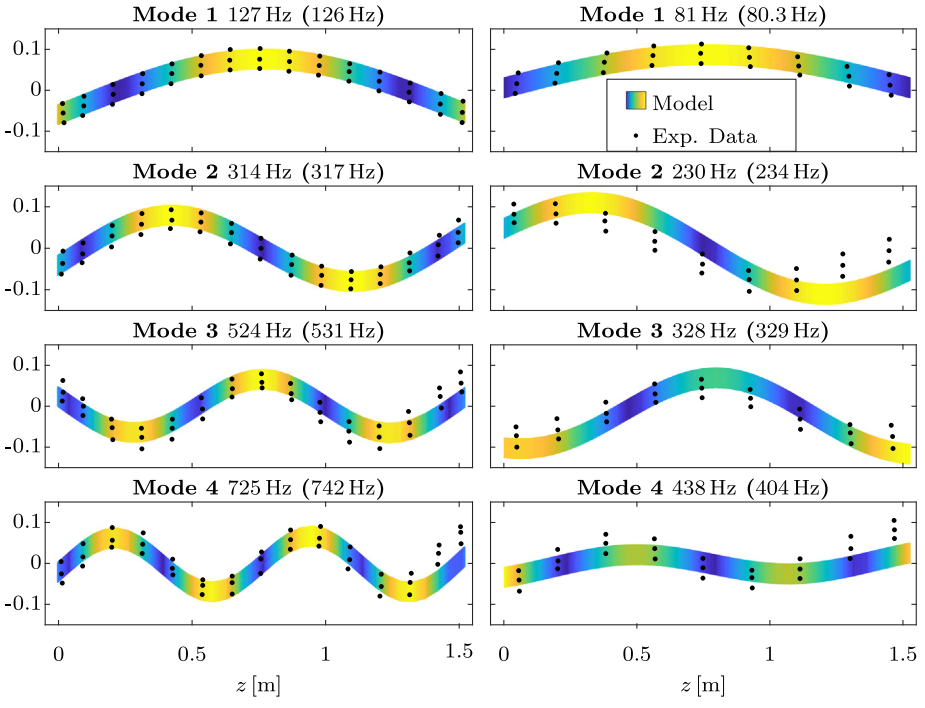

Fig. 7. The shapes of the first four (damped) bending modes in y direction. As the beam is almost symmetric, the modal shapes in x direction are very similar. The bending modes are shown for elastic (left) and bearing (right) supports. The deformation field is normalized for illustration purposes. The experimental values are in brackets.

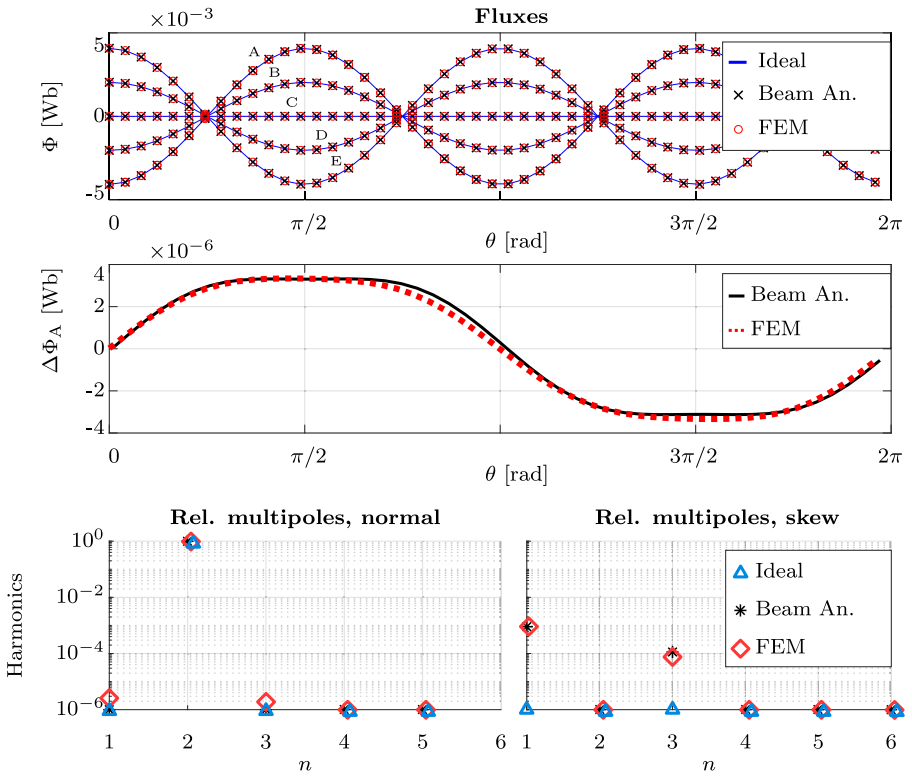

Fig. 8. Simulated flux measurement and spurious multipole content in an ideal quadrupole magnet, considering sag due to gravity. Rotating-coil shaft LHCMMWEQ0489. Top: Absolute signals from the five coils. Middle: Error between quadrupole flux linkage and measurement in the main coil (A) affected by gravity. Bottom: Spurious normal and skew multipole field errors. The coil sag mainly induces spurious skew dipole and sextupole components.

086D20) using medium tips (−20 dB at 700 Hz) and hard tips (−20 dB at 1050 Hz). This ensures the presence of a low frequency input while still exciting the first modes. In fact, for a field measurements, the most critical spectrum is 0–30 Hz.

The coil shaft is mounted on an optical table with a tuned mass-damping system (Newport M-INT4). The measurement system is a 3D vibrometer incorporating the acquisition system (Polytec PSV-400), scanning 45 points on the shaft. Moreover, 4 points on the supports are acquired to validate that its vibrations are negligible. At least six correct[2] impacts are taken per point and the coherence is calculated. The focus is on bending modes, but the axial and torsional modes are also recorded and may be of interest for further improvements of the model.

For elastic supports, the experimental set-up is the one shown in Fig. 5a, and b. The stiffness of the elastic support can be estimated by rigid body modes, because the coil weight is known. This results in $2 \cdot 10^3$ N/m for k_t and $2 \cdot 10^2$ N/m for k_r. The transfer functions of the sample points and modal shapes are obtained directly from the vibrometer acquisition system and compared for both planes. Fig. 6 shows the responses of two points. Fig. 7 (left) shows the normalized modal shapes for the first four bending modes in the y direction. The relative error on the natural frequencies for both directions is 0.013 ± 0.006.

The experimental set-up with the bearings is the same as for the elastic supports. The shaft is now supported by its own bearings; the white rings shown in Fig. 5b. The bearings are made from plastic and their stiffness is estimated minimizing the error on the first natural frequency. The stiffness are $5.5 \cdot 10^6$ N/m for $k_{t,x}$ and $4 \cdot 10^6$ N/m for $k_{t,y}$, while the value of k_r is negligible. The natural frequencies and modal shapes are acquired and compared with the model. They are shown in Fig. 7 (right). The relative error on the natural frequencies for both directions is 0.022 ± 0.028.

4.2. Evaluating the effect on magnetic measurements

A numerical model in COMSOL Multiphysics 5.4 of the existing shaft is created using iso-perimetric, quadrilateral shell elements for both the carbon tube and the PCB. The choice of shell, rather than solid elements, is motivated by the small thickness of the components. Lumped masses and springs are added at the two ends, whose cross-section is assumed to be rigid. Moreover, the transversal bars are modelled as rigid edges. The material properties are given in Table 1.

For the magnetic part of the model, the set of coil and shaft parameters is given in Table 2. The model is validated assuming a perfect quadrupole field described by the harmonic component $B_2(r_0)$. Without loss of generality, r_0 is taken as the geometric centre of the main coil; $r_0 = 0.0403$ m.

The shaft is assumed to be perfectly aligned inside the magnet, with no forces transmitted on the bearings. Eccentricity of the shaft is negligible, thus only the gravity needs to be taken into account. The voltage signals of all five coils are acquired independently. The simulated results are shown in Fig. 8, a comparison between the ideal case, the analytical model, and the FEM simulation. The error between the non-perturbed measurement and the data extracted with a sagging shaft due to gravity is given for the main coil A. The small differences between the analytical model and the FEM analysis are due to micrometre deformations of the PCB, e.g., a small sag in the xy cross-section, that is not predicted by the analytical model. This effect could be modelled by superimposing the effect of a second beam, but a properly assembled rotating-coil can prevent this to happen. The FEM model includes the torsional dynamics and thus allows to verify the decoupling between the bending and torsion.

For the existing shaft, the main spurious harmonics by gravity are the skew dipole and the skew sextupole. The main quadrupole

[2] Correct means that phenomena like double impacts are identified and the related measurements are excluded.

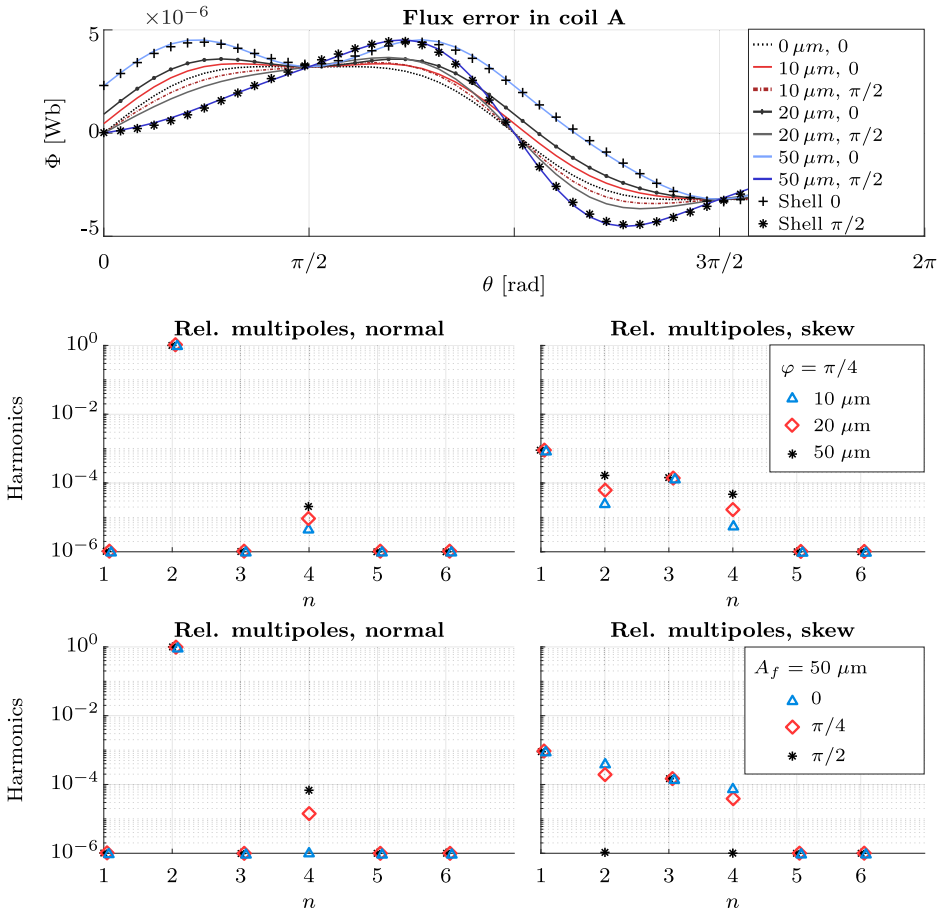

Fig. 9. Simulated measurement of an ideal, prescribed quadrupole field, using a shaft under gravity and vibrations of the bearing at $z = 1.52$. Top: Error between the ideal flux and the measured flux linkage. A comparison with the numerical shell model is shown for the case of maximum vibration. Centre: Harmonic content of coil A, as function of different vibration amplitudes A_v. Bottom: Harmonic content of coil A, as function of different vibration phases φ.

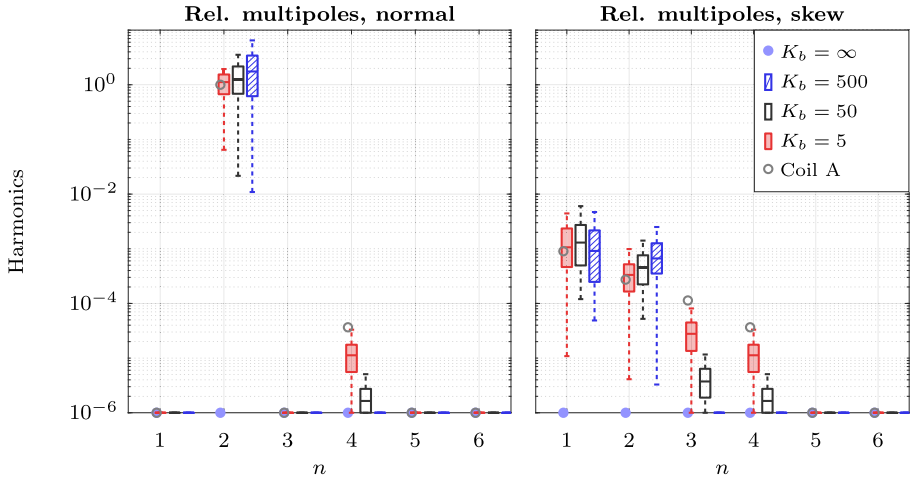

Fig. 10. Simulated measurement of an ideal quadrupole field, using a shaft under gravity and vibrations of the bearing at $z = 1.52\,\text{m}$ of $50\,\mu\text{m}$ at $\pi/4$. Spurious field multipoles as a function of the bucking ratio.

component is measured with a relative error of less than 10^{-4}. This is consistent with the observations published in [7].

5. Sensitivity analysis

The models can now be used with sufficient confidence for a sensitivity analysis of the measurement uncertainty for the absolute signal (coil A) and the multipole field errors in the compensated (bucked) connection scheme of the coils.

5.1. Errors in single-coil measurements

The main effect, in addition to gravity, is the vibration of one extremity, with a harmonic oscillation with an amplitude of up to $50\,\mu\text{m}$. It is introduced in the bearing coordinate frame at different

spatial phases (0 for the x axis and $\pi/2$ for the y axis). The results are shown in Fig. 9 for the analytical beam model and the numerical FEM shell model. The errors on the main field harmonics range between -3×10^{-4} and 3×10^{-4} for 50 µm. The field harmonics most affected by bearing vibration are the skew quadrupole and the octupole. These two high order components arise from unequal spring constants in the x and y directions.

5.2. Effects of bucking

For the rotating-coil shaft LHCMMWEQ0489, the quadrupole bucking scheme is $\Phi = \Phi_A - \Phi_B - \Phi_C + \Phi_D$. This cancels out both the dipole and quadrupole field components. The sensitivity analysis aims at investigating the effects of a non-ideal bucking scheme (not exactly identical coils and non-equidistant spacing). The effectiveness of the compensation is expressed by the bucking factor:

$$K_b := \frac{K_{N,A}}{K_{N,b}}, \tag{25}$$

which is the quotient of the sensitivity of coil A with respect to the main field component N ($N = 1$ for the dipole, $N = 2$ for the quadrupole, etc.), by the sensitivity of the bucked combination of coils with respect to the same component; for ideal bucking $K_b \to \infty$, while in practise, factors around a few hundreds are an achievement. For a quadrupole, for instance, $K_{2,b} = K_{2,A} - K_{2,B} - K_{2,C} + K_{2,D}$. To simulate the sensitivity of the bucking scheme, a set of normally distributed deviations ΔW are added to the width W of each coil. It is applied to the generic case of gravity combined with a vibration of 50 µm at a spatial phase of $\pi/4$. Different bucking levels are evaluated, in particular 5, 50, 500, whose ΔW standard deviations are 2 mm, 250 µm, 40 µm, respectively. Results are given in Fig. 10, including the multipoles from the main coil A. The results show that bucking is effective in reducing the mechanical effects on the measured, higher-order multipoles.

The sensitivity analysis proves that the rotating-coil performs well in terms of mechanical effects. The mechanical dynamics introduces a few units in 10^{-4} of error in the measurements of the main component using coil A. The shaft is also suitable for the measurement of higher-order components with an uncertainty below one unit in 10^{-4} even with a low bucking ratio. This holds for the shaft under investigation, which is made of stiff materials and a large cross-section.

6. Conclusions

Mechanical effects are the most critical source of measurement uncertainty in the operation of a rotating-coil magnetometers. The analytical model presented in this paper describes the main dynamic phenomena related to rigid motion and bending, and allow the calculation of the affect on magnetic measurements. Experimental and numerical validation proves the validity of the model in describing the real shaft mechanics, while the numerical validation proves the validity of the simplifications.

The model allows to quantify parameters in the baseline construction techniques for rotating-coils. First, the model proofs the need for achieving a good bucking ratio. The results confirm also the importance of a good shaft support, in particular the bearings, in order to mitigate vibrations on the shaft. Moreover, it is now possible to quantify how the shaft geometry and materials impact the magnetic measurements, and to calculate the maximum level of vibrations still acceptable for a given measurement system. Because the model is solved in the time domain, it is also possible to simulate transients and non-periodic loads.

The model is also relevant for the design of new shafts with stronger demands on mechanical performance. For example, the model is now adopted to the development of a rotating-coil system mounted on a cantilever frame that is fixed to a linear displacement stage. In this case even small vibrations will be amplified.

CRediT authorship contribution statement

Stefano Sorti: Methodology, Formal analysis, Investigation, Writing - original draft. **Carlo Petrone:** Methodology, Investigation, Resources. **Stephan Russenschuck:** Validation, Supervision, Writing - review & editing. **Francesco Braghin:** Resources, Validation, Supervision.

Declaration of competing interest

The authors declare that they have no known competing financial interests or personal relationships that could have appeared to influence the work reported in this paper.

References

[1] S. Russenschuck, Field Computation for Accelerator Magnets: Analytical and Numerical Methods for Electromagnetic Design and Optimization, Wiley, 2011, URL https://books.google.ch/books?id=tA4VxZvoiJUC.
[2] J. Billan, J. Buckley, R. Saban, P. Sievers, L. Walckiers, Design and test of the benches for the magnetic measurement of the LHC dipoles, IEEE Trans. Magn. 30 (4) (1994) 2658–2661.
[3] N.R. Brooks, L. Bottura, J.G. Perez, O. Dunkel, L. Walckiers, Estimation of mechanical vibrations of the LHC fast magnetic measurement system, IEEE Trans. Appl. Supercond. 18 (2) (2008) 1617–1620.
[4] G. Tosin, J.F. Citadini, E. Conforti, Long rotating coil system based on stretched tungsten wires for insertion device characterization, IEEE Trans. Instrum. Meas. 57 (10) (2008) 2339–2347.
[5] L. Bottura, M. Buzio, P. Schnizer, N. Smirnov, A tool for simulating rotating coil magnetometers, IEEE Trans. Appl. Supercond. 12 (1) (2002) 1680–1683.
[6] P. Arpaia, L. Bottura, V. Inglese, G. Spiezia, On-field validation of the new platform for magnetic measurements at CERN, Measurement 42 (1) (2009) 97–106, http://dx.doi.org/10.1016/j.measurement.2008.04.006.
[7] L. Walckiers, Magnetic measurement with coils and wires, 2011, p. 28, http://dx.doi.org/10.5170/CERN-2010-004.357, Comments: 29 pages, 26 figures, presented at the CERN Accelerator School CAS 2009: Specialised Course on Magnets, Bruges, 16–25 June 2009. For higher-resolution figures see http://cdsweb.cern.ch/record/1340995, URL https://cds.cern.ch/record/1345967.
[8] J. Zhou, W. Kang, S. Li, Y. Liu, Y. Liu, S. Xu, X. Guo, X. Wu, C. Deng, L. Li, Y. Wu, S. Wang, AC magnetic field measurement using a small flip coil system for rapid cycling AC magnets at the China Spallation Neutron Source (CSNS), Nucl. Instrum. Methods Phys. Res. A 880 (2018) 80–86, http://dx.doi.org/10.1016/j.nima.2017.10.040, URL http://www.sciencedirect.com/science/article/pii/S0168900217311166.
[9] I. Ecsedi, A. Baksa, Analytical solution for layered composite beams with partial shear interaction based on Timoshenko beam theory, Eng. Struct. 115 (2016) 107–117, http://dx.doi.org/10.1016/j.engstruct.2016.02.034, URL http://www.sciencedirect.com/science/article/pii/S014102961600122X.
[10] J. Boisson, F. Louf, J. Ojeda, X. Mininger, M. Gabsi, Analytical approach for mechanical resonance frequencies of high-speed machines, IEEE Trans. Ind. Electron. 61 (2014) 3081–3088, http://dx.doi.org/10.1109/TIE.2013.2272282.
[11] O. Ozsahin, H. Ozguven, E. Budak, Analytical modeling of asymmetric multi-segment rotor – bearing systems with Timoshenko beam model including gyroscopic moments, Comput. Struct. 144 (2014) 119–126, http://dx.doi.org/10.1016/j.compstruc.2014.08.001.
[12] D.C.D. Oguamanam, G.R. Heppler, The effect of rotating speed on the flexural vibration of a Timoshenko beam, in: Proceedings of IEEE International Conference on Robotics and Automation, Vol. 3, 1996, pp. 2438–2443.
[13] L. Majkut, Free and forced vibration of Timoshenko beams described by single difference equation, J. Theoret. Appl. Mech. 47 (2009).
[14] G. Genta, Dynamics of Rotating Systems, Springer-Verlag New York, 2005.
[15] G.R. Cowper, The shear coefficient in Timoshenko's beam theory, J. Appl. Mech. 33 (2) (1966) 335–340, http://dx.doi.org/10.1115/1.3625046, arXiv:https://asmedigitalcollection.asme.org/appliedmechanics/article-pdf/33/2/335/5447638/335_1.pdf.
[16] F. Gruttmann, W. Wagner, Shear correction factors in Timoshenko's beam theory for arbitrary shaped cross-sections, Comput. Mech. 27 (2001) 199–207, http://dx.doi.org/10.1007/s004660100239.
[17] E.L. Wilson, Static and Dynamic Analysis of Structures, Computers and Structures, Inc., Berkeley, California, USA, 2004.
[18] S. Russenschuck, G. Caiafa, L. Fiscarelli, M. Liebsch, C. Petrone, P. Rogacki, Challenges in extracting pseudo-multipoles from magnetic measurements, Internat. J. Modern Phys. A 34 (36) (2019) 19, http://dx.doi.org/10.1142/S0217751X19420223, 1942022.
[19] H. Van der Auweraer, Structural dynamics modeling using modal analysis: applications, trends and challenges, in: Proceedings of the 18th IEEE Instrumentation and Measurement Technology Conference. Rediscovering Measurement in the Age of Informatics (Cat. No. 01CH 37188), Vol. 3, IMTC 2001, 2001, pp. 1502–1509.
[20] Z. Li, M.J. Crocker, A study of joint time-frequency analysis-based modal analysis, IEEE Trans. Instrum. Meas. 55 (6) (2006) 2335–2342.